

1. INTRODUCTION

Some important fluids, like water, honey (Sharma, 2013), and molten tellurium, gallium, antimony and bismuth (Ezan & Kalfa 2016), have an anomalous behavior in specific temperature intervals, showing a negative coefficient of thermal expansion. The point where the curve of density as a function of temperature has a local maximum is usually called a density inversion point. For liquid water, this point corresponds to approximately 4° C. Analysis of natural convection involving fluids with density inversion are relevant to several engineering and environmental systems, as for example crystal growth, electronics and foods cooling, ice melting and oceanic and atmospheric circulation (Quintino *et al.* 2017; Hossain & Rees 2005; Li *et al.* 2013). The non-linear dependence of density on temperature makes the fluid dynamics and heat transfer during the natural convection rather complex, as analyzed by several authors in the past decades.

For example, Mirzaie and Lakzian (2006) considered several different arrangements for heat sources/sinks in cavities and solved the governing equations using the Boussinesq approximation and considering the nonlinear dependence of density on temperature. The results show that the Boussinesq approximation tends to overestimate the heat transfer. For some cases, the average Nusselt number almost duplicate in comparison with the non-Boussinesq model, showing the importance of considering the temperature-dependent properties.

Li and Hu *et al.* (Li *et al.* 2015; Hu *et al.* 2016; Hu *et al.* 2017; Hu *et al.* 2017) published a series of studies evaluating Rayleigh-Bénard convection of water near its density inversion point in cylindrical and rectangular cavities. In Li *et al.* (2015) the authors reported the existence of several steady flow patterns in a cylindrical cavity with aspect ratio 2, using a density inversion parameter to define the point of maximum density. The influence of the aspect ratio was later investigated in Hu *et al.* (2016), where the authors verified that the flow patterns depend strongly on the aspect ratio. The existence of multiple stable flow patterns was also observed for a rectangular cavity with aspect ratio 2 (Hu *et al.* 2017a), in particular near to the convection threshold. The authors reported the existence of periodic and unstable convection for higher Rayleigh number values, which was also observed for cylindrical containers (Hu *et al.* 2017b).

Density inversion also plays an important role in water freezing and melting (Ezan & Kalfa 2016; Yoon *et al.* 2001; Kumar *et al.* 2017). Yoon *et al.* (2001) experimentally analyzed the freezing mechanisms of supercooled water at different cooling rates. Three freezing mechanisms were observed depending on the cooling rate, resulting in different distribution and growth rates for ice crystals. The authors indicate that secondary convection caused by density inversion is the root cause for the different mechanisms. The presence of distinct regimes was also observed by Kumar *et al.* (2017), ranging from pure conduction to sustained convection.

In several useful applications, natural convection is not induced by a hot boundary condition. Instead, it can be generated by an internal discrete heat source (Fontana *et al.* 2011; Fontana *et al.* 2013; Fontana *et al.* 2015; Baudoin *et al.* 2017; Siavashi *et al.* 2017; Duluc & Fraigneau 2017). Depending on the geometrical configuration and distribution of the heat sources, the flow pattern can be very complex, as reported in Fontana *et al.* (2015), where the natural convection of air in a partially open cavity with internal heat source was investigated. Even considering the relatively simple thermal behavior of the fluid (ambient air), different periodic and quasi-periodic regimes were observed due to the competition of buoyancy forces induced by the heat sources and shear forces induced by the inflow.

For fluids without a density inversion point, the heat sources can be placed to either stabilize (heated from above, for example) or destabilize the system. However, the density inversion causes a significant change in the system dynamics, since the sources can stabilize for a defined temperature range and destabilize for others. Most of the studies reported in the literature using near-freezing water consider simple geometrical configurations, with the heat sources treated as boundary conditions, which usually leads to relatively simple steady states after an initial transient period. This approach can oversimplify the problem for several applications, where periodic and unsteady states can appear for a certain range of values of the governing parameters. Understanding how these regimes affect the heat transfer is crucial in order to properly configure the system for specific applications, as for example maximize the heat removal. To obtain this information, transient analysis of the flow field is necessary, which drastically increase the computational cost.

Moreover, most of the authors consider closed cavities with boundary conditions at different temperatures, so that the fluid is confined in a finite space. In several important engineering applications, the fluid can leave the system as a result of the flow field, as for example in solar energy collectors, electrical systems, nuclear reactors and heat exchangers. Depending on the ambient and operational conditions, these devices can use water near 4°C as the working fluid, as for example heating of ambient water in cold climates or liquid cooling systems. The presence of openings significantly changes the heat management in these devices, since the incoming and outgoing fluids transport thermal energy in and out of the system. Depending on the configuration, this mechanism can or cannot be significant to the overall thermal control, therefore it is important to define the relevance of each mechanism of heat transfer in order to obtain the best performance.

The objective of this study is to evaluate transient natural convection in an open cavity containing discrete heat sources and initially filled with pure liquid water at the freezing point, aiming to define the main characteristics of the heat transfer and fluid flow as a function of the heat dissipation rate. The nonlinearity of the system of governing equations

Table 1 Coefficients for the temperature-dependent physical properties (Eq. (4))

Property (ϕ)	$\rho(\text{kgm}^{-3})$	$\mu(\text{Pa s})$	$c_p(\text{kJ kg}^{-1}\text{K}^{-1})$	$k(\text{W m}^{-1}\text{K}^{-1})$
ϕ_0	9.9984E+02	1.7913E-03	3.0832E-10	5.6108E-01
$A \times K$	6.7262E-02	-6.2053E-05	-3.4319E-03	1.8936E-03
$B \times K^2$	-8.9516E-03	1.6339E-06	1.2265E-04	2.0372E-06
$C \times K^3$	8.8520E-05	-3.1446E-08	-2.4631E-06	-1.7437E-07
$D \times K^4$	-6.8087E-07	3.0832E-10	2.4392E-08	5.8595E-10

increases the complexity and the computational time required to numerically solve these equations. Using the heat dissipation rate as a control parameter, different flow regimes will be classified and grouped qualitatively according to the main flow characteristics, allowing to a better understanding of the heat transfer mechanisms and making possible to optimize the system configuration for desired applications.

2. MATHEMATICAL MODEL

The physical configuration considered is presented in Fig. 1. The domain consists of an open cavity with discrete heat sources. The top and bottom walls are kept at 0°C and the external fluid is liquid water at 0°C. The solid part containing the heat sources is positioned at the vertical center of the cavity, with the sources divided into 2 sections occupying 1/5 of the total solid volume each section. In this study, it is assumed that $L = 0.1\text{m}$ and $H = L/5$. Initially, the system is considered in a stationary state (no flow) at 0°C. This configuration was chosen to investigate the buoyancy-opposing and the buoyancy-assisted conditions at the same time, depending on the maximum temperature at the heat sources. Moreover, this is a common configuration that can appear in the analysis of electronic devices.

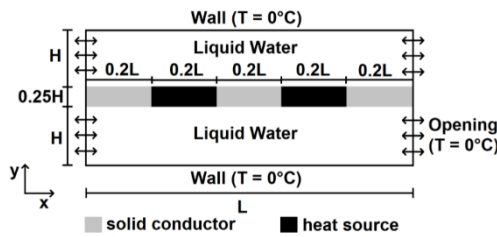


Fig. 1. Scheme of the solution domain and boundary conditions.

The governing equations for the fluid phase are the common continuity, Navier-Stokes and energy conservation equations, expressed, respectively, as:

$$\frac{\partial \rho}{\partial t} + \nabla \cdot (\rho \vec{v}) = 0 \quad (1)$$

$$\frac{\partial (\rho \vec{v})}{\partial t} + \nabla \cdot (\rho \vec{v} \vec{v}) = -\nabla p + (p - p_0)g\vec{j} +$$

$$\nabla \cdot (\mu (\nabla \vec{v} + (\nabla \vec{v})^T - \frac{2}{3}(\nabla \cdot \vec{v})\mathbf{I})) \quad (2)$$

$$\frac{\partial (\rho c_p T)}{\partial t} + \nabla \cdot (\rho c_p T \vec{v}) = \nabla \cdot (k \nabla T) \quad (3)$$

where ρ , μ , c_p and k are, respectively, the fluid density, viscosity, thermal capacity and thermal conductivity, \vec{v} is the velocity vector, t is the time, T is the temperature, p is the pressure, ρ_0 is the reference density (density associated with the reference state $T_{\text{ref}} = 0^\circ\text{C}$), g is the gravitational acceleration and \vec{j} is the unit vector in the y -direction. Therefore, the Boussinesq approximation is not used in this study and the dependence of physical properties on temperature is taken into account. These properties were evaluated using the polynomial fit:

$$\phi = \phi_0 + AF + BT^2 + CT^3 + DT^4 \quad (4)$$

Where the temperature T is given in °C and the coefficients ϕ_0 and $A - D$ are given in Table 1 for each thermophysical property. The coefficients are multiplied by a factor involving the absolute temperature (K) to make it dimensionally consistent with the data presented in Eq. (4). The coefficients were adjusted based on the thermodynamic data presented in the NIST Chemistry WebBook (Lemmon *et al.* 2017), for the temperature range 0°C – 40°C.

For the solid phase, the energy conservation equation can be expressed as:

$$\frac{\partial (\rho_s c_{p,s} T)}{\partial t} = \nabla \cdot (k_s \nabla T) + S_Q \quad (5)$$

where ρ_s , $c_{p,s}$ and k_s are, respectively, the density, thermal capacity and thermal conductivity of the solid phase. For the heat source, these properties were considered as $\rho_s = 2702\text{kgm}^{-3}$, $c_{p,s} = 903\text{J kg}^{-1}\text{K}^{-1}$ and $k_s = 237\text{Wm}^{-1}\text{K}^{-1}$, and for the solid conductor the properties were considered as $\rho_s = 8933\text{kgm}^{-3}$, $c_{p,s} = 385\text{J kg}^{-1}\text{K}^{-1}$ and $k_s = 401\text{Wm}^{-1}\text{K}^{-1}$, corresponding to a heat source made of aluminum and solid conductors made of copper. The source term S_Q corresponds to the volumetric rate of heat dissipation in the heat sources. It is assumed that $S_Q = 0$ in the solid conductors. This parameter will be varied in the range $S_Q = 2 \times 10^5 - 2.2 \times 10^6\text{W/m}^3$ in order to identify different flow regimes.

To measure the heat transfer between the solid walls and the fluid it is evaluated the average Nusselt number, defined here as:

$$Nu = \frac{1}{L} \int_0^L \frac{\partial \theta}{\partial y^*} dx \quad (6)$$

where $y^* = y/H$ is the dimensionless y -direction and θ is the dimensionless temperature, given by:

$$\theta = \frac{T - T_{ref}}{T_{max} - T_{ref}} \quad (7)$$

where T_{max} is the maximum temperature in the system for a given S_Q value. A negative Nusselt number represents the heat transfer from a hot fluid to a cold wall. To determine the intensity of the recirculations it is evaluated the average vorticity in each layer:

$$\bar{\omega} = \frac{1}{HL} \int_0^L \int_{y_0}^{y_f} \|\nabla \times \vec{v}\| dy dx \quad (8)$$

For the lower layer, $y_0 = 0$ and $y_f = H$, while for the upper layer $y_0 = 1.25H$ and $y_f = 2.25H$. To facilitate the presentation of the results, the average vorticity will be presented in a dimensionless form:

$$\omega = \frac{\bar{\omega} L^2}{\alpha_0} \quad (9)$$

Where $\alpha_0 = k_0/\rho_0 c_p$, α_0 is the thermal diffusivity evaluated at the reference state.

The flow is assumed to be laminar. As boundary conditions, at the top and bottom walls it was assumed no-slip and no-penetration conditions (normal and tangential components of the velocity vector are set as zero) and the temperature is fixed at 0°C. At the interface between the fluid and the heat sources/solid conductors it is also assumed no-slip and no-penetration conditions for the Navier-Stokes equation, however, for the energy conservation it is considered continuity of the heat flux. The left and right boundaries are considered as openings, allowing the fluid to enter or leave the system, depending on the pressure gradient. No external force is applied, therefore, the flow direction and intensity are defined based on the forces generated by the natural convection inside the system. The external fluid is considered as liquid water at 0°C.

The set of governing equations and the respective boundary conditions were solved using the CFD package ANSYS CFX 16.0, where the equations are discretized using an element-based finite volume method. This software is a well-established tool in the study of natural convection with discrete heat sources (Xu *et al.* 2017; Fontana *et al.* 2013; Lu *et al.* 2016). Different mesh sizes were evaluated to test the convergence of the numerical method. In Fig. 2 it is presented a comparison between the temperature along the centerline of the lower layer ($y = H/2$) obtained with meshes of different size. As can be seen, the curve for a mesh with 290×340 elements (in y and x directions, respectively) is almost identical to the curve for a mesh with 355×450 elements. Therefore, the mesh with 290×340 elements was used in the simulations. The curves presented in Fig. 2 were obtained considering $S_Q = 2.2 \times 10^6 \text{W/m}^3$, however, for lower S_Q values the behavior is similar. The number of iterations was fixed in order to achieve a convergence criteria with

average residual of 10^{-6} .

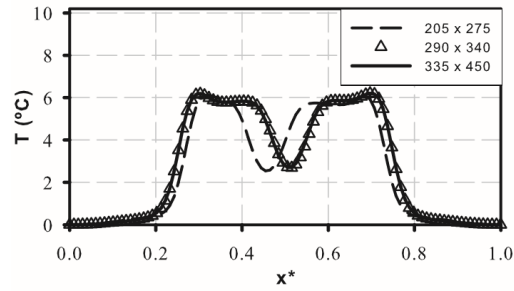


Fig. 2. Temperature along the centerline of the lower layer ($y = H/2$) for $S_Q = 2.2 \times 10^6 \text{W/m}^3$ and different mesh sizes.

To verify the code performance, a comparison with benchmark cases reported in Mastiani *et al.* (2017) and Michalek & Kowalewski (2005) was carried out, where the natural convection of water near the density inversion point is investigated in a closed square cavity with a side length of 38 mm. The vertical walls kept at different temperatures (0°C for the left wall and 10°C for the right wall), while the horizontal walls were treated as adiabatic. Michalek and Kowalewski (2005) used a modified version of the FREVON3V software, where the finite difference method is used with a false transient approach to solving the Navier-Stokes and energy conservation equations for laminar flow. Mastiani *et al.* (2017) solved the governing equations with the ANSYS Fluent software, where the finite volume method is applied with a multigrid strategy to discretize the governing equations. The authors used the SIMPLE algorithm to solve the pressure-velocity coupling. Figure 3 compares the velocity profiles obtained in this study and the results re-reported by Mastiani *et al.* (2017) and by Michalek and Kowalewski (2005). The results are presented in a dimensionless form ($u^* = uL_c/\alpha_0$ and $v^* = vL_c/\alpha_0$, where L_c is the length of the cavity and u and v are the horizontal and vertical components of the velocity vector) and correspond to the profiles evaluated at the central line. As can be observed, the curves obtained show a remarkable agreement with the values reported in the literature. Further-more, Michalek and Kowalewski (2005) found an average Nusselt number of 6.5 using a mesh with 380×380 elements, while the value found in the present study was $Nu = 6.532$.

Furthermore, to verify the physical consistency of the mathematical model proposed, a comparison with experimental results presented by Banaszek *et al.* (1999) was performed, as shown in Fig. 4, where the vertical velocity evaluated at different y^* values is presented. The physical configuration, in this case, is the same used for the results reported in Fig. 3 (square cavity with vertical walls at 0°C and 10°C). The authors used particle image velocimetry techniques combined with digital color analysis to acquire the velocity and temperature fields, using a thermochromic liquid crystal as seeding. As can be seen in Fig. 4, the numerical results represent very well the experimental data. The small deviation

observed close to $x^* = 0.6$ for $y^* = 0.25$ (Fig. 4-a) and close to $x^* = 0.7$ for $y^* = 0.5$ (Fig. 4-b) was also noticed by [Banaszek *et al.* \(1999\)](#). According to the authors, this deviation is due to heat transfer through the bottom and top walls, considered in the mathematical model as adiabatic.

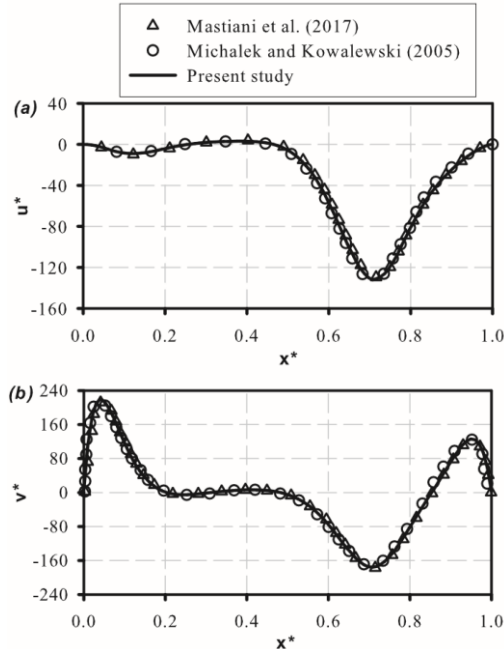


Fig. 3. Comparison with numerical results reported in [Mastiani *et al.* \(2017\)](#) and [Michalek and Kowalewski \(2005\)](#) for (a) horizontal velocity and (b) vertical velocity.

3. RESULTS

In order to identify the different flow regimes, 21 cases were analyzed for S_Q values in the range $10^5 - 2.2 \times 10^6 \text{W/m}^3$. Table 2 presents an overview of the flow characteristics observed for each case, based on the configuration observed in the lower and upper layers. This classification was done to facilitate the discussion of the results and was based on qualitative differences between the cases. Table 2 also presents the maximum temperature (T_{max}) reached inside the system, including the solid parts.

In the upper layer, the increase in density as the temperature increases (in the range $0 - 4^\circ\text{C}$) tends to stabilize the fluid and a stable conductive regime can be observed for low S_Q values. When the maximum temperature reaches approximately 9.8°C ($S_Q = 1.25 \times 10^6 \text{W/m}^3$), the conductive configuration loses its stability and the flow becomes unstable. Further increasing the heat source intensity in the interval analyzed do not change the flow configuration in this layer. It is worth noting that no steady convective regime was observed in the upper layer.

The lower layer behavior is rather more complex. For low S_Q values, the increase in the density at the fluid/heat sources interface creates a steady convective regime. As the S_Q value increases, different periodic regimes were observed. The flow

field and energy distribution characteristics significantly change depending on the flow regime. In the following sections, each of these regimes will be analyzed individually.

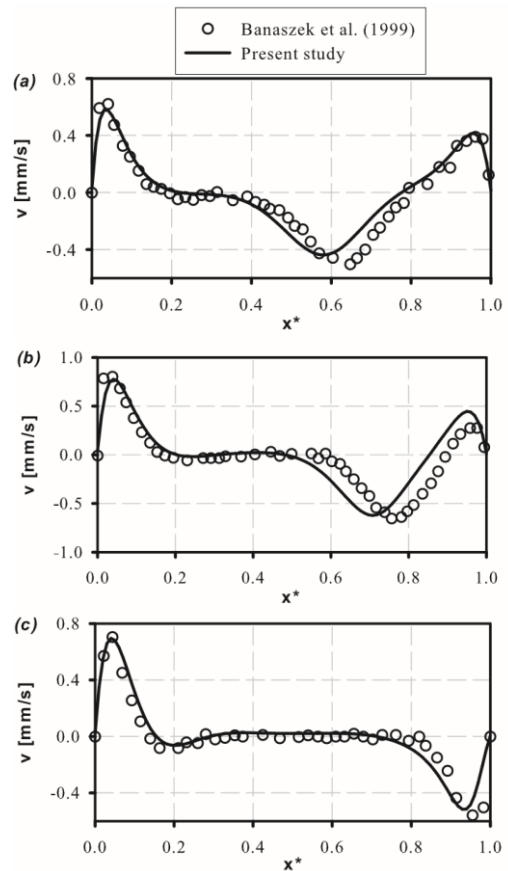


Fig. 4. Comparison with experimental results reported in [Banaszek *et al.*](#) for vertical velocity evaluated at (a) $y^* = 0.25$, (b) $y^* = 0.5$ and (c) $y^* = 0.75$.

3.1 Regime 01 - Stable convection/Conduction

The first regime observed after a pure conductive state corresponds to steady convection in the lower layer (heated from above) and conduction in the upper layer (heated from below). This is a fairly simple configuration, where after an initial transient state all the variables reach a steady state. A small recirculation region due to the opening conditions appears in the upper layer, however, this will not be considered as a convective state. Instead, the transition between conduction/convection will be defined as a result of a significant change in the flow field induced by the heat sources.

Figure 5 illustrates the transient behavior of the average temperature in each layer (Fig. 5-a) and the average temperature at the opening (Fig. 5-b) for Case 2 ($S_Q = 2 \times 10^5 \text{W/m}^3$). The temperature is measured in degrees Celsius, in order to facilitate the identification of the density inversion point (4°C). In all figures, the time is presented in a dimensionless form $t^* = \alpha_0/L^2$.

The average temperature is greater in the lower layer due to the increase in the heat transfer coefficient at

Table 2 Flow regimes for different S_Q values.

Case	Regime	$S_Q(\text{W/m}^3)$	$T_{\max}(\text{°C})$	Lower layer	Upper layer
1	1	1×10^5	1.107	Steady convection	conduction
2	1	2×10^5	1.982	Steady convection	conduction
3	2	3×10^5	2.755	stable periodic	conduction
4	2	4×10^5	3.484	stable periodic	conduction
5	2	5×10^5	4.131	stable periodic	conduction
6	2	6×10^5	4.810	stable periodic	conduction
7	2	7×10^5	5.472	stable periodic	conduction
8	3	8×10^5	6.158	doubly periodic	conduction
9	3	9×10^5	6.855	doubly periodic	conduction
10	3	1×10^6	7.585	doubly periodic	conduction
11	3	1.1×10^6	8.382	doubly periodic	conduction
12	3	1.2×10^6	9.523	doubly periodic	conduction
13	4	1.25×10^6	9.792	quasi-periodic	unsteady
14	4	1.3×10^6	9.926	quasi-periodic	unsteady
15	4	1.4×10^6	10.364	quasi-periodic	unsteady
16	5	1.5×10^6	10.776	weakly periodic	unsteady
17	5	1.6×10^6	11.237	weakly periodic	unsteady
18	6	1.7×10^6	11.741	Steady convection	unsteady
19	6	1.8×10^6	12.241	Steady convection	unsteady
20	6	2×10^6	13.284	Steady convection	unsteady
21	6	$2.21.107 \times 10^6$	14.416	Steady convection	unsteady

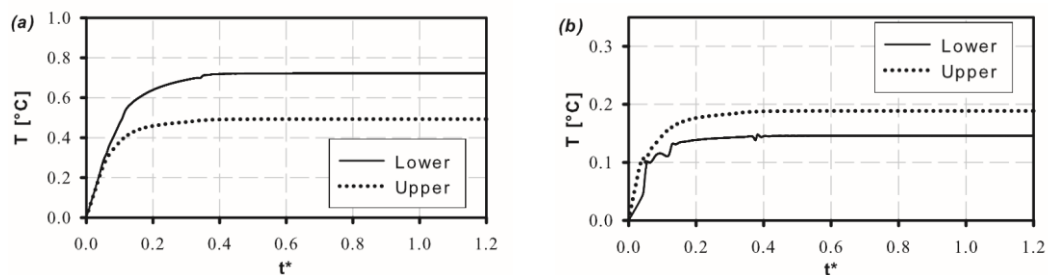


Fig. 5. Transient evolution of (a) average temperature and (b) average opening temperature in both layers for Case 2.

the heat source/fluid interface, caused by the convective motion. Nevertheless, the temperature at the opening is greater in the upper layer. The curves of mass flow through the opening will not be presented, but it is worth to mention that the mass flow is slightly greater in the upper opening as well, indicating that more energy leaves the system through the upper openings than through the lower openings. The second mechanism of heat removal is through the heat transfer with the cold horizontal top/bottom walls. A detailed analysis of the temperature field shows that the average Nusselt number is greater in the bottom wall, therefore the fact that more energy leaves the system through the upper openings, even considering the greater average temperature in the lower layer, does not contradict the energy conservation principle. The results for Case 1 are similar and will not be presented for the sake of brevity. This procedure will be maintained in

the following sections, where the results obtained for one representative case will be used to characterize a particular regime.

3.2 Regime 02 - Stable periodic/Conduction

When the heat source is increased to $S_Q = 3 \times 10^5 \text{W/m}^3$, a periodic state is observed, as illustrated in Fig. 6 for Case 7. Figure 6-a shows the dimensionless temperature evaluated at the central point of each layer ($x = L/2$ and $y = H/2$ for the lower layer and $y = 1.75H$ for the upper layer), while Fig. 6-b shows the average dimensionless vorticity in each layer.

In this case, after an initial unsteady state the lower layer changes to a periodic state. The dimensionless period of oscillation \bar{T} in this case is $\bar{T} \approx 0.01$. The upper layer, on the other hand, remains in a conductive steady state. As well as observed for Case

2, the fluid/wall heat transfer is more significant at the bottom wall than at the top wall, with $Nu \approx -2.27$ at the bottom wall and $Nu \approx -0.012$ at the top wall. Due to the increase in the convective motion, the average vorticity is greater in the lower layer. Even though the upper layer is classified as a conductive state, the vorticity is not zero due to a small mass flow at the openings.

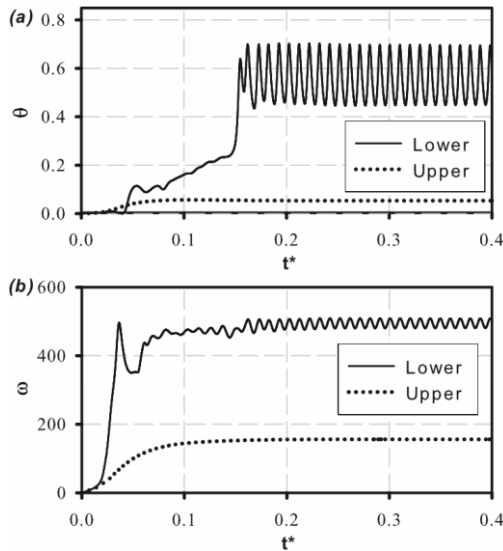


Fig. 6. Transient evolution of dimensionless (a) temperature and (b) vorticity for Case 7.

To illustrate the physical behavior during an oscillation, Fig. 7 shows the dimensionless temperature (θ) for different times based on an arbitrary value t_0 , corresponding to a crest in the curve of θ as a function of time. In the upper layer the fluid remains in the base conductive state, while in the lower layer, after the initial unsteady state, the convective motion is established, where the hot and denser fluid descends in the central part while the cold fluid enters through the upper part of the opening and moves horizontally towards the middle part.

As the cold incoming fluid moves, a wave-like instability develops close to the heat source wall. The incoming fluid is less dense than the fluid in the boundary layer next to the wall. The presence of shear forces in a continuous layer of fluid with a density gradient causes the development of waves, which is the same mechanism observed in the Kelvin-Helmholtz instability. In this case, there is a layer of more dense fluid close to the wall, and as the less dense fluid flows under this layer with a different velocity, small perturbations at the interface are amplified, causing the flow instability and the appearance of waves. When the crest of this wave reaches the middle part ($x = L/2$), an upside-down mushroom structure is formed (Fig. 7-a). This structure, however, is not sustained for long. As the wave trough approaches the center, part of the hot fluid detaches from the mushroom-shaped structure, as observed in Fig. 7-c. This fluid moves towards the opening, causing an oscillatory behavior in the

Nusselt number at the bottom wall as well. After a sufficiently long time, the system returns to its original configuration, closing the cycle.

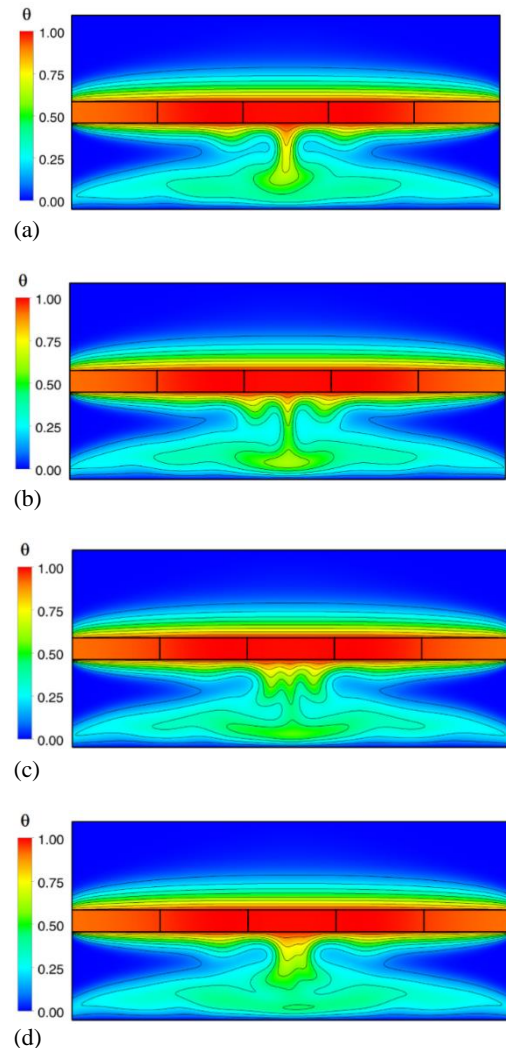


Fig. 7. Variation in θ profile during a cycle for Case 7, evaluate at (a) $t^* = t_0$, (b) $t^* = t_0 + \bar{T}/4$, (c) $t^* = t_0 + \bar{T}/2$ and (d) $t^* = t_0 + 3\bar{T}/4$.

3.3 Regime 03 - Doubly periodic/Conduction

Further increasing the heat dissipation rate S_Q , the lower layer enters in a slightly different regime, defined as doubly periodic. This is also a periodic state, however, there are two different amplitudes in the oscillation, as observed in Fig. 8, where the dimensionless temperature is presented for a specific time interval for Case 10 ($S_Q = 10^6 \text{W/m}^3$). Even though there are two oscillations in the cycle, the period is reduced to $\bar{T} \approx 0.009$. The oscillation amplitude is also significantly smaller compared with Case 7. Due to this small amplitude, the doubly periodic regime cannot be clearly observed in the curves for the average values of the variables, therefore these curves will not be presented. The average Nusselt number at the bottom and top walls are still around -2.27 and 0.012 , respectively.

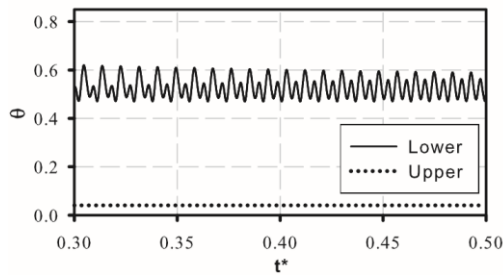


Fig. 8. Transient evolution of dimensionless temperature evaluated at the central point of each layer for Case 10.

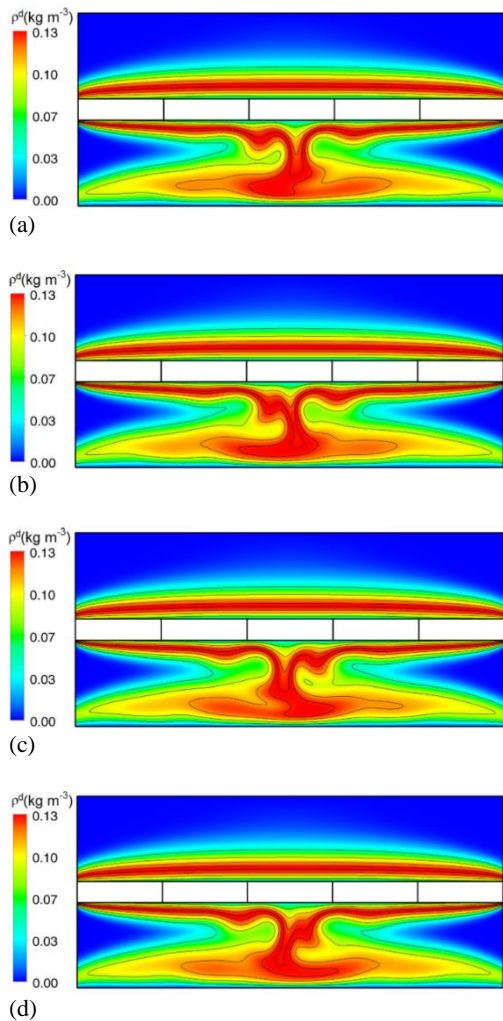


Fig. 9. Variation in density profile during a cycle for Case 10, evaluated at (a) $t^* = t_0$, (b) $t^* = t_0 + 0.28\bar{T}$, (c) $t^* = t_0 + 0.58\bar{T}$ and (d) $t^* = t_0 + 0.8\bar{T}$.

The origin of the periodic state for Case 10 is similar to the mechanism described for Case 7. The main difference is that a symmetry break is observed for Case 10, as illustrated in Fig. 9. To facilitate the visualization of the buoyancy forces, this figure shows profiles of fluid density in both layers. The density is presented as the deviation from the reference state, $\rho^d = \rho - \rho_0$. In the upper layer, the point of maximum density is not adjacent to the wall, which could turn the conductive state unstable due to

the Rayleigh-Taylor instability or even due to natural convection induced by the Rayleigh-Bénard mechanism. However, in this case, the viscous forces are strong enough to keep the system stable.

In the lower layer, there is also the development of a wavy flow close to the heat source walls due to the presence of a shear flow. The presence of a significant density gradient close to the heat source walls can be clearly visualized in this case. However, differently from Case 7, the waves in the right and left parts are out of phase, causing a symmetry break. It is important to note that based only on these CFD results, it is not possible to precise the origin of the phase displacement in the waves, therefore the possibility of numerical oscillations cannot be completely eliminated. Nevertheless, the results indicate that a perturbation in one of the sides can be amplified causing a symmetry break. Based on the results presented in Fig. 9, it is possible to identify that the two crests seen in the curve of θ (Fig. 8) are a direct result of the out-of-phase wavy flow close to the heat sources. Moreover, the reduction in the amplitude of the oscillations in comparison with Case 7 can also be understood, since there is no more a constructive interference of the waves traveling in opposite directions.

3.4 Regime 04 - Quasi-periodic/Unsteady

The increase in the heat source from $S_Q = 1.2 \times 10^6 \text{W/m}^3$ to $S_Q = 1.25 \times 10^6 \text{W/m}^3$ induces a significant change in the flow characteristics. The temperature increase at the heat sources makes the buoyancy forces in the upper layer become strong enough to surpass the stabilization effect of the viscosity and an unsteady convective motion takes place. In the lower layer, the configuration becomes even more complex and a stable periodic regime is no longer observed. Instead, the system presents a quasi-periodic behavior, as illustrated in Fig. 10-a, where the time evolution of θ is shown for Case 14. After an initial period, the temperature starts to oscillate around an average value. This oscillation, however, does not have a specific frequency, as observed in previous cases.

To better understand the phenomena associated with his case, Fig. 11 shows the variation in the Fluid density for different t^* values. Fig. 11-a corresponds approximately to the point of maximum observed in Fig.10-a for $t^* \approx 0.5$. In the lower layer, the fluid enters through the upper part of the opening, flows towards the middle and descends at the central part, similarly to the observed for the previous cases. However, near to the center of the bottom wall, the fluid becomes lighter and buoyancy forces generate an ascending plume that causes a reduction in θ . This plume has its peak at $t^* \approx 0.6$, which correspond to a point of minimum in Fig. 10-a. At the same time, the descending denser fluid tends to oppose this flow, generating an oscillation. This process is not always identical, which makes the average values erratically oscillate around an average value, as seen in Fig. 10.

In the upper layer, as previously mentioned, there is the appearance of unsteady flow. Close to the heat sources, the fluid becomes sufficiently light and

penetrative convection originates thermal plumes, similar to the Rayleigh-Taylor instability. As these plumes ascend, the layer of denser fluid is displaced and originate a contrary force, restraining the propagation of the thermal plumes. Thus, the convective region is restricted to approximately the bot-tom half of the upper layer. This restriction causes the average vorticity to be significantly smaller in the upper layer. As the S_Q value is increased, the buoyancy forces become more intense and the extension of the thermal plumes also increases. Due to the formation of the plumes, the Nusselt number at the heat sources/fluid interface in the upper layer increases and becomes of the same order of the Nu in the lower layer (Fig. 10-c).

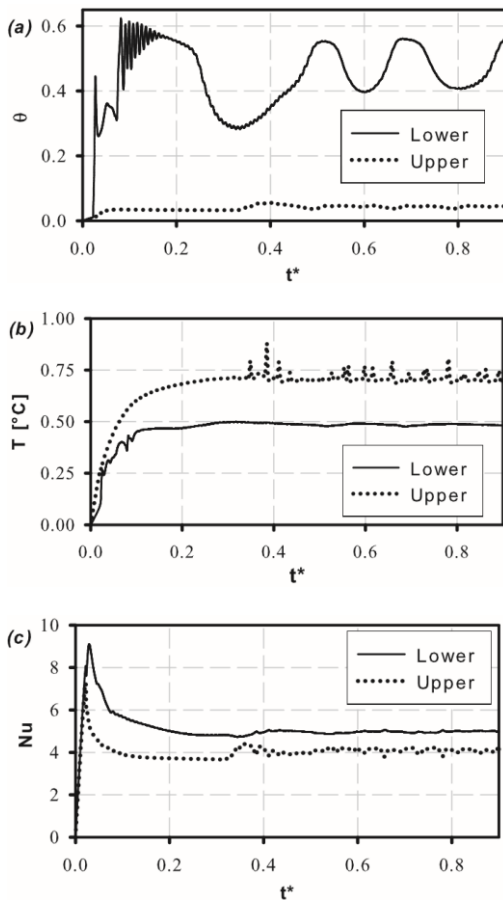


Fig. 10. Transient evolution of (a) θ at the central point, (b) average opening temperature and (c) Nu at the source/fluid interface for Case 14.

The thermal plumes are formed near the central part of the upper layer and move toward the opening as the time progress. This phenomenon generates the peaks exhibited in Fig. 10-b, where the average temperature of the fluid at the opening is presented. Moreover, it is interesting to notice that in the upper layer the fluid close to the heat sources moves from the center to the opening, while in the lower layer the flow is in the opposite direction. At the lower layer, the heat transfer between the hot fluid and the bottom cold wall causes a reduction in the opening temperature when compared with the upper layer.

3.5 Regime 05 - Weakly-Periodic/Unsteady

For a small interval, including $S_Q = 1.5 \times 10^6 \text{W/m}^3$ and $S_Q = 1.6 \times 10^6 \text{W/m}^3$, the lower layer returns to exhibit a periodic behavior, as illustrated in Fig. 12-a, where the time evolution of θ at the central point is presented for Case 16. In this case, the amplitude of the oscillations is much smaller than for the previous cases, therefore, this regime is identified as weakly-periodic in order to distinguish from the previous ones.

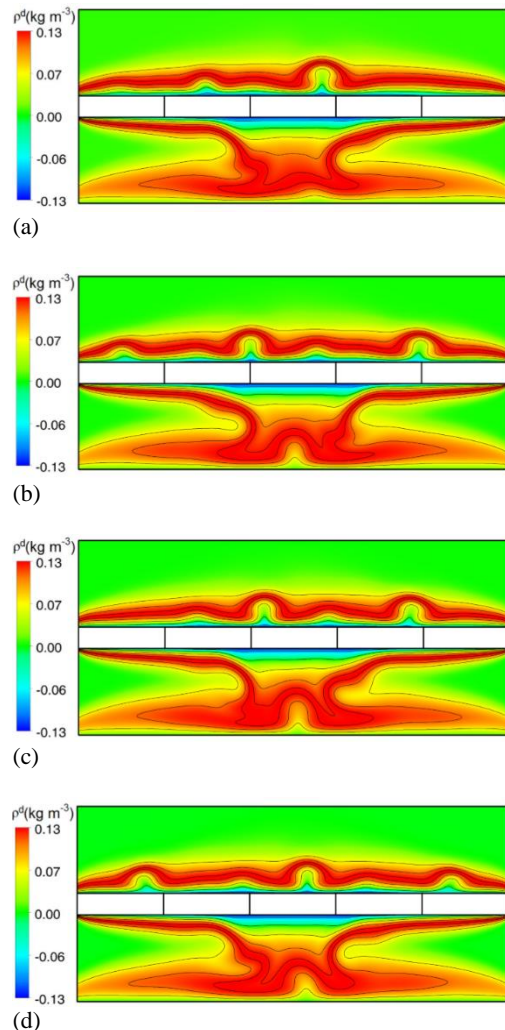


Fig. 11. Variation in density profile with time for Case 14, evaluated at (a) $t^* = 0.5$, (b) $t^* = 0.55$, (c) $t^* = 0.6$ and (d) $t^* = 0.65$.

A significant change occurs in the time evolution of θ in the upper layer, as seen in Fig. 12-a. Previously, the thermal plumes do not have a significant influence in the middle point, however, for $S_Q = 1.5 \times 10^6 \text{W/m}^3$ the buoyancy forces are strong enough to affect the entire bottom half of the upper layer. Apart from this difference, the general behavior of the upper layer is very similar to the observed for the previous case. The superior part of the upper layer remains at the initial temperature, resulting in very small Nu values at the top wall, while at the bottom wall it reaches values around -2.25 . Even so, the Nu at the source/fluid interface reaches practically the

same values in both layers, as shown in Fig. 12. As expected, the vorticity in the upper layer also increases and reaches values of the same order as in the upper layer, as presented in Fig. 12-c.

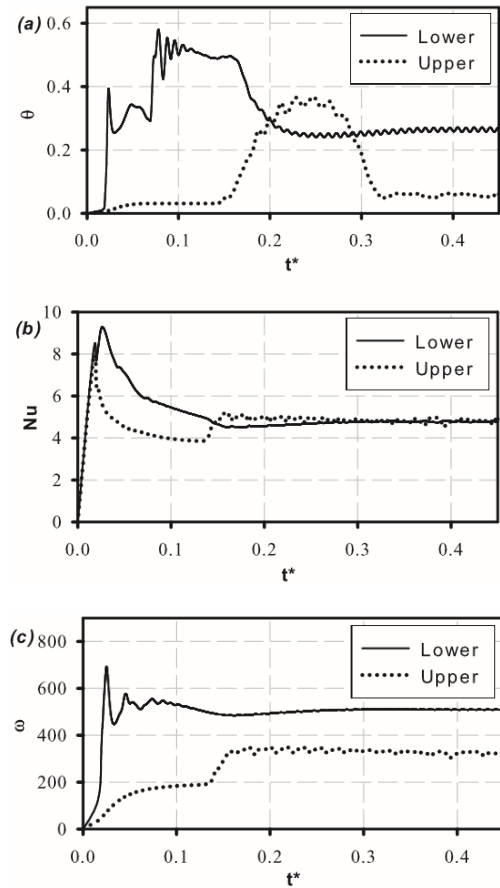


Fig. 12. Transient evolution of (a) θ at the central point, (b) Nu at the source wall and (c) average vorticity for Case 16.

As previously stated, the lower layer shows a periodic behavior, with a period of oscillation of $\bar{T} \approx 0.009$. In the regime previously discussed (Regime 4), it was mentioned the existence of a quasi-periodic ascending flow close to the central part of the bottom wall (see Fig. 11). For Case 16, this flow becomes more intense and originates a small recirculation zone where the fluid ascends through the central part, becomes heavier as it is heated and then starts to descend. The energy is provided by the descending fluid heated by the heat sources and, as previously discussed, there is the formation of small waves close to the solid walls, thus creating the periodic flow.

3.6 Regime 06 - Steady Convection/Unsteady

For heat dissipation rates higher than $1.7 \times 10^6 \text{W/m}^3$, the final regime observed correspond to steady convection in the lower layer and a highly unsteady motion in the upper layer. Figure 13 shows the time evolution of θ at the central point and the average temperature at the opening for both layers, where it is possible to verify that, after an initial transient state, the lower layer reaches a stationary state, while

in the upper layer the average values erratically oscillate around value. It is important to note that no periodic or unsteady regime is observed in the lower layer, indicating that a stable convective configuration is established.

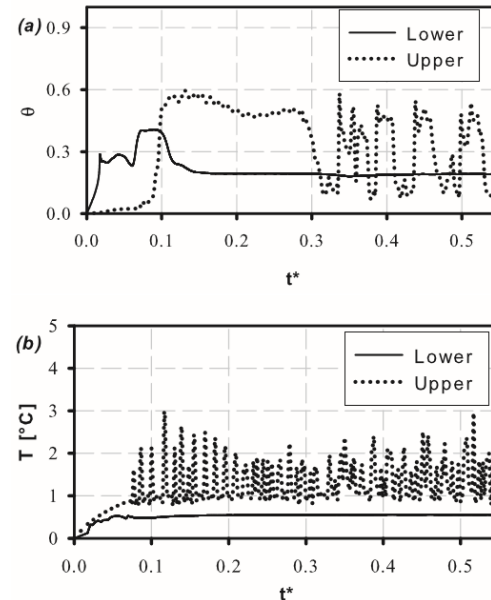


Fig. 13. Transient evolution of (a) θ at the central point and (b) average temperature at the opening for Case 18.

The frequency of thermal plumes formation in the upper layer increases significantly, as can be verified in Fig. 13-b. As these plumes are displaced from the central part to the openings, they transport the thermal energy released and facilitate the heat removal, causing the greater average opening temperature in the upper layer. The mass flow through the openings is similar in both layers, which indicates that more energy leaves the system through the upper openings. Even considering that the heat transfer with the cold top/bottom wall is more significant in the lower layer, the average temperature in the upper layer is around 3.25°C and around 4.8°C in the lower layer. Moreover, for this case the Nu at the heat sources is bigger in the upper layer than in the lower layer, indicating that more heat is transferred to the upper layer. The unsteady flow in the upper layer also increases expressively the vorticity, reaching values even bigger than in the lower layer.

Figure 14 shows θ profiles for different t^* values. In the upper layer, the thermal plumes are formed throughout the entire solid interface, since the temperature gradient in the horizontal direction is small due to the solid high thermal conductivity. These plumes appear erratically, creating a highly non-symmetrical structure as the time progress. In the lower layer, the fluid still enters through the upper part of the opening, but in this case, the distance that the fluid flows adjacent to the heat source walls is greatly reduced and the wavy flow is no longer observed. Just after the opening, the

incoming fluid descends and then proceeds to leave the system, making the opening a non-effective mechanism to remove energy. This phenomenon also explains the relatively low opening temperature in the lower layer (Fig. 13-b). In the central region, there is the formation of several recirculating zones. The ascending flow near to the middle point of the bottom wall becomes strong and two secondary ascending regions are formed. The intensity of these secondary flows increases as S_Q increases. The presence of the recirculation regions over a large extension of solid walls difficult the heat transfer, causing an increase in the average temperature and a reduction in the Nusselt number, as previously discussed.

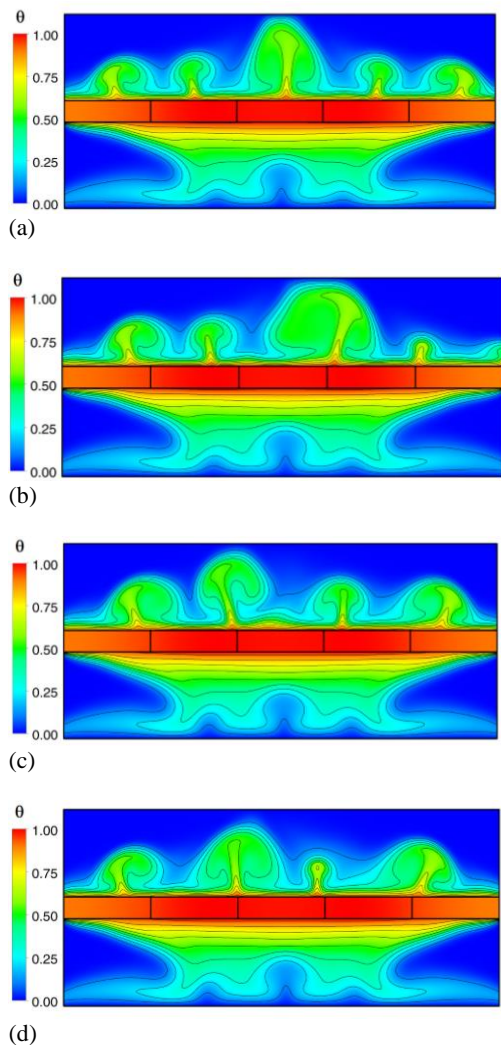


Fig. 14. Variation in dimensionless temperature profile with time for Case 18, evaluated at (a) $t^* = 0.2$, (b) $t^* = 0.3$, (c) $t^* = 0.4$ and (d) $t^* = 0.5$.

4. CONCLUSIONS

Fluids with a density inversion point, like water at 4°C, exhibit a complex natural convection flow due to the nonlinear dependence of buoyancy forces with temperature. In this case, the Boussinesq approximation cannot be applied and the dependence

of physical properties on temperature must be considered. In this study, it was investigated the natural convection of water near to the density inversion point in a cavity with lateral openings and discrete heat sources. Based on the intensity of heat dissipation rate S_Q , six different flow regimes were observed.

In the upper layer (heated from below), for small S_Q values the heat transfer occurs basically by conduction since the initial increase of density with temperature tends to stabilize the system. When S_Q is sufficiently high, the buoyancy forces generate thermal plumes that occupy part of the upper layer. It is important to notice that Rayleigh-Bénard instabilities were not observed in the upper layer, even considering that it is a layer heated from below and cooled from above. The plumes developed in the upper layer are displaced horizontally due to the influence of the opening and the hot fluid is removed from the system. This horizontal component of the velocity hinders the development of the cells.

The general behavior of the lower layer is rather more complex, with different periodic regimes appearing for specific S_Q intervals. These regimes arise as a result of waves formation in the fluid as it enters through the opening and flows toward the central part. The interference pattern of these waves creates periodic flow configurations and significantly affect the dynamics of the heat transfer in the lower layer.

Comparing the heat removal through the openings and the heat transferred to the cold walls, it was possible to verify that the presence of openings is a more efficient mechanism of energy removal in the upper layer, while heat transfer with the cold horizontal wall is much more important in the lower layer. The top cold wall just plays a significant influence for high S_Q values, when the convective plumes are strong enough to surpass the opposing hydrostatic forces and reach the top wall. Therefore, depending on the system configuration (heated from above or below) and the intensity of heat dissipation, the most adequate mechanism of heat control can be chosen.

ACKNOWLEDGMENTS

The authors would like to thank CNPq (Conselho Nacional de Desenvolvimento Científico e Tecnológico - Brazil) through the processes 303906/2015-4, 405101/2016-3 and 407625/2016-0 for the financial support.

REFERENCES

- Banaszek, J., Y. Jaluria, T. A. Kowalewski, and M. Rebow (1999). Semi-implicit FEM analysis of natural convection in freezing water. *Numerical Heat Transfer, Part A* 36, 449 – 472.
- Baudoin, A., D. Saury, and C. Bostrom (2017). Optimized distribution of a large number of power electronics components cooled by conjugate turbulent natural convection. *Applied*

- Thermal Engineering* 124, 975 – 985.
- Duluc, M. C. and Y. C. Fraigneau (2017). Effect of frequency on natural convection flows induced by a pulsating line-heat source. *International Journal of Thermal Sciences* 117, 342 – 357.
- Ezan, M. A. and M. Kalfa (2016). Numerical investigation of transient natural convection heat transfer of freezing water in a square cavity. *International Journal of Heat and Fluid Flow* 61, 438 – 448.
- Fontana, E., A. Silva, and V. C. Mariani (2011). Natural convection in a partially open square cavity with internal heat source: An analysis of the opening mass flow. *International Journal of Heat and Mass Transfer* 54, 1369 – 1386.
- Fontana, E., C. A. Capeletto, A. Silva, and V. C. Mariani (2013). Three-dimensional analysis of natural convection in a partially-open cavity with internal heat source. *International Journal of Heat and Mass Transfer* 61, 525 – 542.
- Fontana, E., C. A. Capeletto, A. Silva, and V. C. Mariani (2015). Numerical analysis of mixed convection in partially open cavities heated from below. *International Journal of Heat and Mass Transfer* 81, 829 – 845.
- Hossain, M. A. and D. A. S. Rees (2005). Natural convection flow of water near its density maximum in a rectangular enclosure having isothermal walls with heat generation. *Heat Mass Tran.* 41, 367 – 374.
- Hu, Y. P., Y. R. Li, and C. M. Wu (2016). Aspect ratio dependence of Rayleigh-Bénard convection of cold water near its density maximum in vertical cylindrical containers. *International Journal of Heat and Mass Transfer* 97, 932 – 942.
- Hu, Y. P., Y. R. Li, C. M. Wu, S. Z. Li, and M. H. Li (2017a). Flow pattern and heat transfer in Rayleigh-Bénard convection of cold water near its density maximum in a rectangular cavity. *International Journal of Heat and Mass Transfer* 107, 1065 – 1075.
- Hu, Y. P., Y. R. Li, M. H. Lai, L. Zhang, and S. Z. Li (2017b). Effects of enclosure geometry and thermal boundary condition on Rayleigh-Bénard convection of cold water near its maximum density. *International Journal of Thermal Sciences* 120, 220 – 232.
- Kumar, V., A. Srivastava, and S. Karagadde (2017). Real-time observations of density anomaly-driven convection and front instability during solidification of water. *ASME Journal of Heat Transfer* 140(40).
- Lemmon, E. W., M. O. McLinden, and D. G. Friend (2017). *Thermophysical Properties of Fluid Systems*. Gaithersburg MD: National Institute of Standards and Technology.
- Li, Y. R., Y. P. Hu, and X. F. Yuan (2013). Three-dimensional numerical simulation of natural convection of water near its density maximum in a horizontal annulus. *International Journal of Thermal Sciences* 71, 274 – 282.
- Li, Y. R., Y. P. Hu, Y. Q. Ouyang, and C. M. Wu (2015). Flow state multiplicity in Rayleigh-Bénard convection of cold water with density maximum in a cylinder of aspect ratio 2. *International Journal of Heat and Mass Transfer* 86, 244 – 257.
- Lu, Y., Q. Yu, W. Du, and Y. Wu (2016). Natural convection heat transfer of molten salts around a vertically aligned horizontal cylinder set. *International Communications in Heat and Mass Transfer* 76, 147 – 155.
- Mastiani, M., M. M. Kim, and A. Nematollahi (2017). Density maximum effects on mixed convection in a square lid-driven enclosure filled with Cu-water nanofluids. *Advanced Powder Technology* 28, 197 – 214.
- Michalek, T. and T. A. Kowalewski (2005). Natural convection for anomalous density variation of water: numerical benchmark. *Progress in Computational Fluid Dynamics* 5, 158 – 170.
- Mirzaie, M. and E. Lakzian (2006). Natural convection of Cu-water nanofluid near water density inversion in horizontal annulus with different arrangements of discrete heat source sink pair. *Advanced Powder Technology* 27, 1337 – 1346.
- Quintino, A., E. Rici, S. Grignaffini, and M. Corcione (2017). Heat transfer correlations for natural convection in inclined enclosures-filled with water around its density-inversion point. *International Journal of Thermal Sciences* 116, 310 – 319.
- Sharma, K. (2013). On thermodynamic analysis of substances with negative coefficient of thermal expansion. *Engineering* 5(11), 844 – 849.
- Siavashi, M., V. Bordbar, and P. Rahnama (2017). Heat transfer and entropy generation study of non-Darcy double-diffusive natural convection in inclined porous enclosures with different source configurations. *Applied Thermal Engineering* 110, 1462 – 1475.
- Xu, H., H. H. Chen, S. Wang, Z. Li, K. Li, G. Stecker, W. Pan, J. J. Lee, and C. C. Chen (2017). Coupled natural convection and radiation heat transfer of hybrid solar energy conversion system. *International Journal of Heat and Mass Transfer* 107, 468 – 483.
- Yoon, J. I., C. G. Moon, E. Kim, Y. S. Son, J. D. Kim, and T. Kato (2001). Experimental study on freezing of water with supercooled region in a horizontal cylinder. *Applied Thermal Engineering* 21, 657 – 668.